Nanoscale Advances

ROYAL SOCIETY OF CHEMISTRY

COMMUNICATION

View Article Online
View Journal | View Issue

Cite this: *Nanoscale Adv.*, 2021, **3**, 1375

Received 17th November 2020
Accepted 17th February 2021

DOI: 10.1039/d0na00964d

rsc.li/nanoscale-advances

Investigating the reactive oxygen species production of Rose Bengal and Merocyanine 540-loaded radioluminescent nanoparticles†

Anne Nsubuga, Gabrielle A. Mandl and John A. Capobianco *

Radioluminescent nanomaterials have garnered significant attention in the past decade due to their potential to perform X-ray mediated photodynamic therapy (X-PDT). Many of these materials are assumed to produce singlet oxygen based on a single assay. Herein we demonstrate that multiple assays are required to confidently determine whether singlet oxygen or other reactive oxygen species are being produced through type I or type II PDT mechanisms. Rose Bengal and Merocyanine 540 photosensitizers were loaded into mesoporous silica-coated $NaLuF_4$:Dy^{3+},Gd^{3+} nanoparticles and the combination of ABDA, DPBF, and NaN_3 assays along with electron paramagnetic resonance were employed to determine that superoxide and hydroxyl radicals were exclusively produced from this system under X-ray excitation. Knowledge of the correct PDT mechanism is crucial for informing what types of disease may be best suited for treatment using PDT nanosystems.

Introduction

Radioluminescent (RL) phosphors have garnered significant attention due to their ability to convert ionizing radiation into UV, visible and NIR light. Bulk RL materials are widely used for the detection of ionizing radiation, however, the development of radioluminescent nanoparticles (RLNPs) has transformed the potential applications of radioluminescent phosphors, particularly with respect to biological applications.[1–4] The most promising RLNP compositions utilize lanthanide ions as activators doped into various inorganic hosts such as oxides, tungstates, aluminates, oxysulfides and fluorides, among others.[5–8] Lanthanide-doped nanoparticles based on a fluoride host have attracted considerable attention due to their unique properties, such as wide band gap, low phonon energy, and high chemical and radiation stability.[9,10] Thus, fluoride-based lanthanide-doped nanoparticles have emerged as strong candidates for achieving efficient $4f^n$–$4f^n$ emissions under ionizing excitation.[11,12]

The absorption of X-ray photons by lanthanide-doped nanoparticles results in primary and secondary physical processes, such as the photoelectric effect, Compton scattering, Auger electron emission, X-ray fluorescence and pair production, with varying cross-sectional dependencies on effective atomic number of the material and/or incident X-ray energy.[13,14] The multitude of complex processes that occur in RLNPs upon their excitation with ionizing radiation have been demonstrated to enhance medical treatments such as radiotherapy (RT) and photodynamic therapy (PDT) due to the ability of X-rays and excited secondary electrons to travel distances well beyond the length of a single nanoparticle.[13] Thus, it is possible for a single X-ray photon to excite activator ions in adjacent nanoparticles or target molecules, such as photosensitizers for photodynamic therapy. Furthermore, RLNPs containing high-Z elements, such as Ag, Au, Hf, Lu, or Gd are known to promote the production of reactive oxygen species (ROS) during RT due to their high X-ray absorption cross sections which facilitate a strong reaction with surrounding oxygen and water molecules.[15,16] Recent studies highlight the development of different RLNPs as energy mediators for indirect activation of photosensitizers by using X-rays as an excitation source for PDT, in a process now known as X-PDT.[15,17–20] Conventional PDT utilizes light of a specific wavelength to excite a photosensitizer molecule to its triplet excited state and leading to the production of cytotoxic singlet oxygen and other ROS, such as hydroxyl, hydrogen peroxides and superoxide anion radicals. ROS and singlet oxygen are powerful oxidants that can damage biomolecules such as lipids, proteins and nucleic acids, making PDT a successful treatment for superficial cancers, actinic keratoses, and macular degeneration.[21,22] In the newly developed approach, RLNPs are capable of exciting photosensitizers and inducing the production of singlet oxygen and other ROS in tandem with radiotherapy treatments, which can penetrate deeply below surface tissues.

Department of Chemistry and Biochemistry, Centre for NanoScience Research, Concordia University, 7141 Rue Sherbrooke Ouest, Montreal, QC, H4B 1R6, Canada. E-mail: John.capobianco@concordia.ca

† Electronic supplementary information (ESI) available. See DOI: 10.1039/d0na00964d

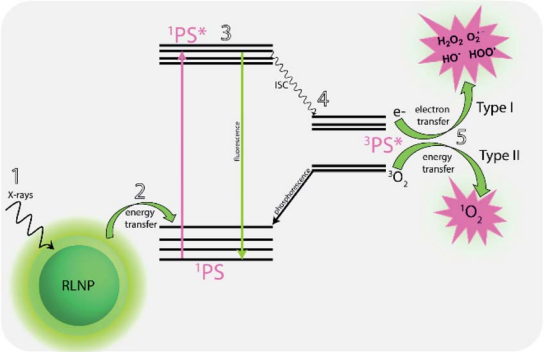

Fig. 1 Schematic of the X-ray mediated photodynamic therapy (X-PDT) process in which (1) a radioluminescent nanoparticle (RLNP) is excited by X-rays. (2) Energy transfer from the nanoparticles excites a photosensitizer to (3) the excited singlet state, after which it can undergo intersystem crossing (4) to the excited triplet state and induce either a type I or type II PDT effect (5).

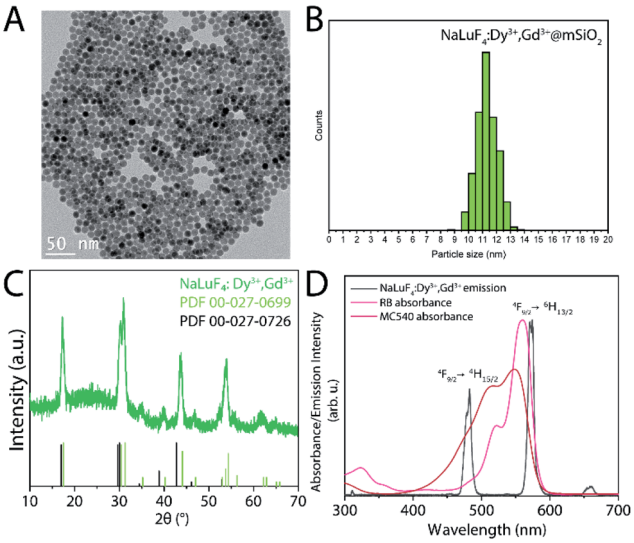

Fig. 2 (A) TEM image of $NaLuF_4$:20% Gd^{3+}, 3% Dy^{3+}@$mSiO_2$ nanoparticles. (B) Size distribution of mesoporous silica coated nanoparticles indicating a size of 11.1 ± 1 nm. (C) Powder X-ray diffraction of the nanoparticles matches the diffraction patterns of $NaLuF_4$ (PDF-00-027-0726) and $NaGdF_4$ (PDF-00-027-0699) hexagonal phases. (D) The radioluminescence emission spectrum (black trace) of the RLNPs overlaps well with the absorbance of RB (pink trace) and MC540 (red trace).

As previously discussed, the ability of X-rays and secondary electrons to travel significant distances results in the potential for excitation of multiple photosensitizers from a single ionization event, potentially improving the PDT effect by a significant amount. ROS species can be produced by type I (*i.e.* $O_2^{\bullet-}$ and H_2O_2 and $^{\bullet}OH$) or type II (*i.e.* $^1O_2$) photochemical reactions (Fig. 1). Most of the clinical applications relating to PDT are based on type II PDT. However, the production of singlet oxygen is highly dependent on oxygen concentration, and unfortunately, the microenvironment in the majority of solid tumours is usually hypoxic. Thus, the combination of a hypoxic environment and simultaneous oxygen consumption during PDT further intensifies oxygen tension, resulting in therapeutic resistance.[23,24] One of the approaches being explored to circumvent this problem is the use of nanomaterials and photosensitizers capable of generating ROS species through type I PDT, which is minimally dependent on intracellular oxygen content.[25]

In the present study, we describe a novel RLNP nanocomposite system which produces type I PDT reactions under X-ray irradiation. Sub-20 nm $NaLuF_4$:20% Gd^{3+}, 3% Dy^{3+} RLNPs were coated with mesoporous silica and loaded with the Rose Bengal (RB) and Merocyanine 540 (MC540). ROS production following X-ray irradiation of the RLNP-PS systems were evaluated using two different commercially available probes, 9,10-anthracenediyl-bis(methylene)dimalonic acid (ABDA) and 1,3-diphenylisobenzofuran (DPBF). ABDA is a fluorescence probe which is specific for singlet oxygen detection, while DPBF is known to react with singlet oxygen, superoxide, hydrogen peroxide, and nitrogen radicals, among others.[26] It is however, worth noting, that DPBF is known to have a higher detection sensitivity for singlet oxygen detection than ABDA.[26] Thus, it is common that results obtained from a DPBF probe experiment alone are assumed to correlate to singlet oxygen production.[27,28] In contrast, electron paramagnetic resonance (EPR) spectroscopy in combination with spin traps can be used to unambiguously determine what species are produced.[29] Furthermore, introduction of sodium azide, an efficient scavenger of singlet oxygen, can be used to confirm the presence or absence of singlet oxygen in the system.

Herein, we demonstrate that it is unlikely that singlet oxygen is the primary ROS produced by the RLNP-PS system in the case of both MC540 and RB. These results highlight the importance of investigating nanoparticle-based PDT systems with multiple probes to ensure an accurate and reliable determination of the PDT mechanism, which can significantly impact the environments in which the system may be more efficient.

Prior to conducting *in vitro* and *in vivo* studies it is primordial to firmly characterize the reaction pathway in order to thoroughly understand how PDT actually works, so that the modulation of its effect can be achieved to maximize the therapeutic outcome. It is only in completely understanding the processes involved that ideal nanomaterials and conditions can be determined for each application.

Results and discussions

Physical characterization of RLNPs and PS loading

β-$NaLuF_4$:20% Gd^{3+}, 3% Dy^{3+} were synthesized following a reported co-precipitation synthesis method with slight modifications.[30] Transmission electron microscopy (TEM) images reveal the as-synthesized nanoparticles display narrow size distribution and excellent monodispersity with an average diameter of 9 ± 1 nm (Fig. 2A, B and S1A, B†). As shown in Fig. 2C, powder X-ray diffraction confirmed that the RLNPs are hexagonal phase, and no other phase or impurities were identified. The RLNPs were coated with mesoporous silica in order to facilitate photosensitizer loading. Silica coating was confirmed by FT-IR

spectroscopy, which exhibits the typical Si–O–Si stretching vibrations (Fig. S2A†).

The N_2 adsorption/desorption isotherm (ESI Fig. S2B†) for the silica-coated nanoparticles can be classified as type IV with a hysteric loop according to the IUPAC classification scheme for mesoporous materials, thus confirming mesoporous silica was coated onto the nanoparticles.

The Brunauer–Emmett–Teller (BET) surface area and average pore size of RLNP@mSiO_2 were 214.94 m^2 g^{-1} and 8.32 nm respectively, suggesting that a large amount of photosensitizer can be loaded due to the high surface area and mesoporous structure. The size of the RLNPs increased from 9 ± 1 nm to 11 ± 1 nm after silica coating, implying a shell thickness of 1 nm (Fig. 2A). Radioluminescence spectroscopy was performed with an unfiltered X-ray beam (Au target) operating at 50 kVp, 80 μA (Fig. 2D). The chosen X-ray energies, in combination with the high Z_{eff} material $NaLuF_4$ were chosen for their potential to provide efficient ROS production.[13] As shown in Fig. 2D, the RL emission spectrum of β-$NaLuF_4$:20% Gd^{3+}, 3% Dy^{3+} exhibited the distinct $4f^n$–$4f^n$ transitions from Dy^{3+} ions from the $^4F_{9/2}$ excited level to the ^6H_J (J = 15/2 and 13/2) levels, located at 484 and 573 nm, respectively. The absorption spectrum of the PS overlaps well with the emissions from Dy^{3+}. Thus, it is expected that following X-ray excitation of RLNPs, RB and MC540 would be activated *via* an energy transfer process to produce ROS.

The amount of loaded PS was determined using UV-vis absorption spectroscopy and BET analysis. The average surface loading was determined to be 1.062 × 10^{15} molecules RB per cm^2, and 5.658 × 10^{12} molecules MC540 per cm^2. The decreased loading amount for MC540 is expected since MC540 is a larger molecule than RB and will occupy more surface area.[31,32]

Control studies

Suspensions of RLNPs (2 mg mL^{-1}) loaded with MC540 or RB in 50/50 v/v DMSO/H_2O or DMSO/D_2O were evaluated using DPBF and ABDA. DMSO/D_2O and DMSO/H_2O were chosen as solvent systems to accommodate the stability of the nanoparticles as well as solubility of DBPF, which is insoluble in neat water.[26] Furthermore, D_2O was used as a solvent system to increase the lifetime of singlet oxygen, thus allowing for more likely detection of singlet oxygen if it were formed. It has been demonstrated that the X-ray energy deposited to an aqueous suspension of nanoparticles is mostly deposited to the solvent during the primary interaction phase.[13] The energy attenuated by the water molecules then results in secondary production of Auger electrons and secondary X-rays, which can then interact with the nanoparticles; this has been implicated in a decreased type II photodynamic effect in nanoparticle-facilitated X-PDT applications.[13] Thus, to facilitate as much primary energy deposition to the nanoparticles as possible, the irradiated nanoparticle suspension had a depth of 0.5 cm to prevent total attenuation of X-rays by the solvent near the surface of the sample. Additionally, the suspension was stirred during irradiation to increase the homogeneity of the dose deposited to the entire contents of the sample. All samples were irradiated for a total of 5 minutes, with UV-Visible absorption spectra measured at 30 second intervals during the irradiation.

Control experiments were performed on solutions of MC540 and RB under X-ray excitation with and without DPBF or ABDA as a ROS or singlet oxygen probe to evaluate the possibility of direct photosensitization of MC540 and RB, as well as the potential for PS or DPBF/ABDA degradation under ionizing radiation. Neither PS nor the DPBF or ABDA solutions alone exhibited degradation during the 5 minute irradiation experiments, as evidenced by the minimal changes in the absorption maxima of both PSs and probes (Fig. 3A and B). A slight decrease in the DPBF absorption was observed for the MC540 and RB samples without nanoparticles present, indicating a small degree of ROS production during X-ray excitation, likely due to the radiolysis of water. It has been previously demonstrated that MC540 and RB do not exhibit direct photosensitization upon irradiation with X-rays due to the mismatch in excitation energy required to form the excited triplet states of these molecules, in line with our observations.[33,34] Finally, a solution of RLNPs@mSiO_2 without any photosensitizers was irradiated with X-rays in the presence of DPBF or ABDA, and a small decrease in both DPBF and ABDA absorbance was observed. Thus, the RLNPs@mSiO_2 alone appear to induce ROS and singlet oxygen production, likely due to the radiolysis of water during the irradiation of all the samples with X-rays.

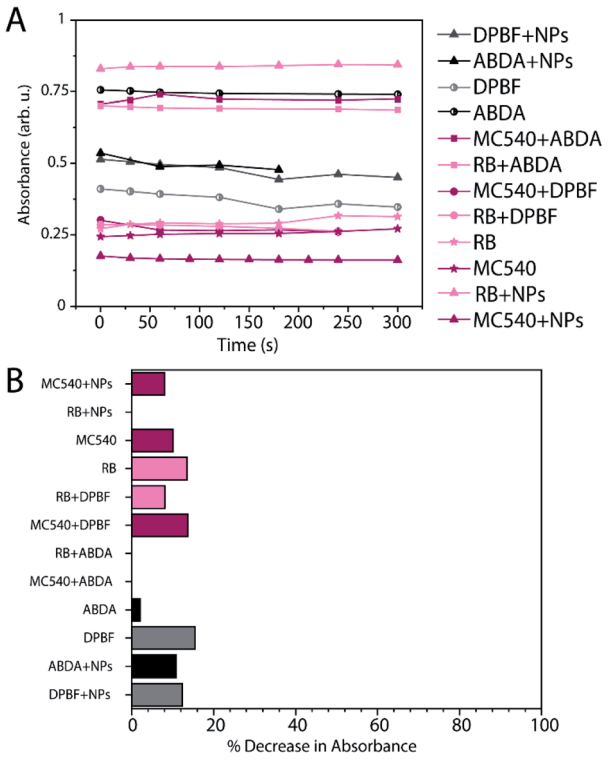

Fig. 3 (A) Graph of the UV-Visible absorption maxima of control samples *vs.* time illustrating the difference in absorbance after 5 minutes (300 seconds) of X-ray irradiation. λ_{max} DPBF: 416 nm, λ_{max} ABDA: 400 nm, λ_{max} RB: 565 nm, λ_{max} MC540: 553 nm. (B) Percent decrease of λ_{max} of each sample after 5 minutes of X-ray irradiation.

Based on the control results, any decrease in absorbance of DPBF or ABDA during the actual experiments had to be more than 15% for the results to be considered significantly different (Fig. 3B).

Finally, the stability of the RB and MC540-loaded RLNP systems were evaluated for 48 hours and no appreciable leakage was observed over this time course (sub-5% release after 48 hours). Thus, it can be expected that efficiency of energy transfer between the nanoparticles and photosensitizers would remain unchanged during the duration of the experiments (Fig. S5†).

Evaluation of $^1O_2$ and ROS production using ABDA, DPBF and sodium azide assays

Evaluation of singlet oxygen production of the RB-RLNP@mSiO_2 system using ABDA as a probe revealed an ABDA absorbance decrease of 2% and 1.5% for the RB-RLNP@mSiO_2 system in DMSO/H_2O (sample RAH) and DMSO/D_2O (sample RAD), respectively after 5 minutes, which could not be considered significant (Fig. 4A and B). In contrast, evaluation of the ROS production using the DPBF probe resulted in a 68% decrease in absorbance for the sample RDH, and a 11% decrease in the DPBF absorbance for the RDD sample (Fig. 4C and D). Similar results were obtained for experiments performed with MC540-loaded RLNPs@mSiO_2. Experiments utilizing ABDA as a probe indicate insignificant singlet oxygen production for the MC540-RLNPs in DMSO/D_2O (MAD) and DMSO/H_2O (MAH) as evidenced by a sub-0.5% decrease in the ABDA absorbance (Fig. 4A). However, using the DPBF probe, again resulted in a large percent decrease in DPBF absorbance (Fig. 4B). A 60% decrease in the DPBF signal was observed in the DMSO/H_2O sample (MDH), and a 14% decrease in the DMSO/D_2O (MDD) sample. The substantial decrease in DPBF signals for both PS-RLNP systems, after only 5 minutes of X-ray irradiation, represents a significant improvement in ROS or singlet oxygen generation over several other reported systems when considering their singlet oxygen probe assay results (Fig. S7A and B†).[19,28] The significantly larger decrease in the DPBF absorbance in both samples, relative to ABDA, can be attributed to two possibilities. First, DPBF is known to be more sensitive as a singlet oxygen probe and could thus be more efficient at detecting singlet oxygen.[26] Second, singlet oxygen may not be the primary ROS produced, as evidenced by the insignificant decrease in ABDA absorbance, which is singlet oxygen-specific.

To determine if singlet oxygen was being produced, the experiments were repeated with the same concentrations of PS-loaded nanoparticles, and DPBF, but with 20 mM NaN_3 included in the solution. Sodium azide is a well-known singlet oxygen scavenger;[5,35] if singlet oxygen is produced by the nanoparticles, the rate of DPBF quenching should decrease and subsequently the absorbance should decrease to a lesser extent. No significant change in the rate or percentage of DPBF absorbance decrease was observed with and without NaN_3 for both PS-RLNP systems, as shown in Fig. 5A and B.

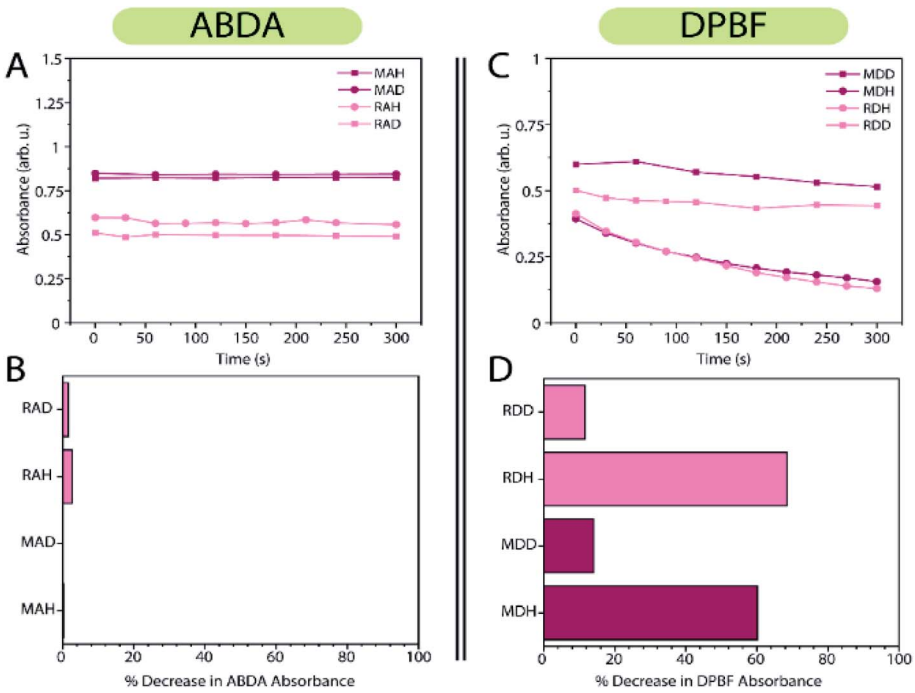

Fig. 4 (A) Graphical depiction of absorbance maximum of MC540-RLNPs + ABDA in DMSO/H_2O (MAH), MC540-RLNPs + ABDA in DMSO/D_2O (MAD), RB-RLNPs + ABDA in DMSO/H_2O (RAH) and RB-RLNPs + ABDA in DMSO/D_2O (RAD) as a function of irradiation time. (B) Percent decrease in absorbance of ABDA as a function of irradiation time of the samples in (A). (C) Graphical depiction of absorbance maximum of MC540-RLNPs + DPBF in DMSO/D_2O (MDD), MC540-RLNPs + DPBF in DMSO/H_2O (MDH), RB-RLNPs + DPBF in DMSO/H_2O (RDH) and RB-RLNPs + DPBF in DMSO/D_2O (RDD) as a function of irradiation time. (D) Percent decrease of DPBF absorbance as a function of irradiation time of the samples in (C). All samples were irradiated with 50 kVp, 80 μA X-rays (Au target, unfiltered) for a duration of 5 minutes.

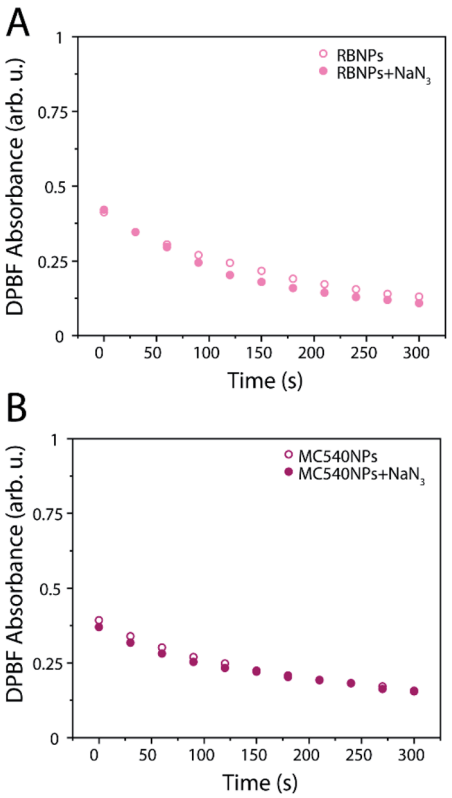

Fig. 5 Absorbance maximum of DPBF as a function of irradiation time of a solution of (A) RB-RLNPs (2 mg mL^{-1}) and (B) MC540-RLNPs with and without 20 mM sodium azide as a function of irradiation time.

Thus, it can be confidently concluded that the lack of ABDA quenching with either PS-NP system is because no appreciable amount of singlet oxygen is being produced in either case. Both systems were found to exhibit the photodynamic effect through a type I mechanism. Additionally, it is worth noting that the RB and MC540 absorbance signals decreased as a function of irradiation time when the same experiment is performed with a direct excitation of 532 nm (Fig. S6A and B†). The production of singlet oxygen is known to cause irreversible photobleaching of RB and MC540.[36,37] Importantly, no decrease in the RB and MC540 signals were observed during the X-ray excitation experiments, indicating no photobleaching occurred (ESI Fig. S4A and B†). The type I photoreactions that occur with RB to form superoxide anions also result in the formation of RB radical anions which undergo reversible reactions to regenerate neutral RB molecules.[36] The lack of degradation of RB or MC540 during the X-ray experiments is further evidence that the type I reaction is favored under these conditions.[38]

Electron paramagnetic resonance studies

To further understand the type I reactions occurring in both PS-RLNP systems, EPR spectroscopy was carried out. EPR spectroscopy allows qualitative determination of ROS formation and identification of ROS species through the use of a diamagnetic spin trap that forms relatively stable spin adducts with paramagnetic parameters that depend on the nature of the trapped radical.[29] The spin trap 3,3,5,5-tetramethylpyrroline-*N*-oxide (TMPO) can react selectively with superoxide to produce a spin adduct designated TMPO–OOH.[39] A dispersion of RB-RLNPs or MC540-RLNPs in DMSO/H_2O was exposed to X-rays, and the EPR spectra were subsequently recorded. The obtained spectra exhibit a characteristic 1 : 1 : 1 : 1 quartet signal having hyperfine splitting constants (hfsc, $a_N = 14$ G, $a_{H\beta} = 6.5$ G), indicating the generation of the TMPO–OOH adduct for both systems (Fig. 6A and B).[39] Aiming to confirm the presence of other

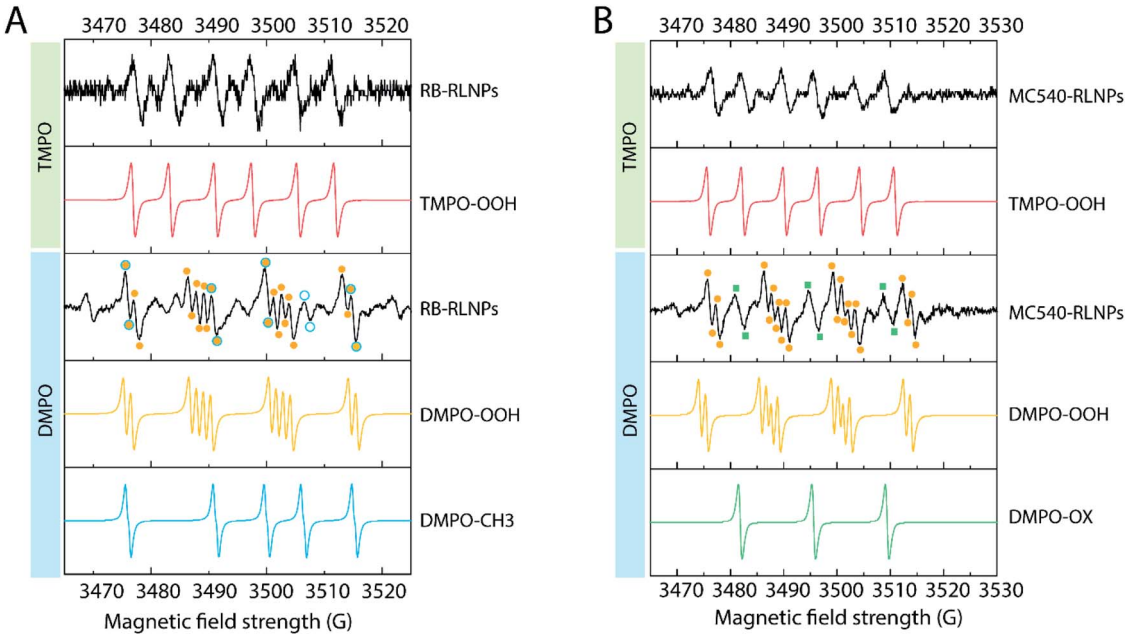

Fig. 6 Electron paramagnetic resonance studies of (A) RB-RLNPs with TMPO or DMPO and the corresponding simulated adducts. (B) MC540-RLNPs with TMPO or DMPO and the corresponding simulated adducts.

reactive oxygen species, a second set of EPR experiments were carried out using the 5,5-dimethyl-pyrroline *N*-oxide (DMPO) spin trap. DMPO was chosen as it is used to identify oxygen-centered radicals, *e.g.* superoxide anion, peroxyl, alkoxyl, and hydroxyl radicals; the resulting spin adducts of each species have distinct spectral signals.[40,41] The interaction of the short-lived superoxide anion radicals with DMPO yields the DMPO–OOH adduct (Fig. 6A and B). The spectrum obtained from spin-trapping experiments with DMPO reveal signals that can be attributed to the DMPO–OOH adduct, confirming the results from the TMPO experiment. The hyperfine coupling constants ($\alpha_N = 13.2$ G, $\alpha_{H\beta} = 11.0$ G, and $\alpha_{H\gamma} = 0.8$ G) are consistent with previously reported values for the DMPO–OOH adduct.[42]

Additionally, we confirmed hydroxyl radical generation in the RB-RLNP system. As shown in Fig. 6A, the spectra also feature signals that can be assigned to the formation of the DMPO–CH_3 adduct (with hyperfine constant $a_N = 16.4$ mT, $a_{H\beta} = 23.4$ mT). The production of DMPO–CH_3 adduct is initiated by hydroxyl radicals, which rapidly react with DMSO (eqn (1) and (2)), thus confirming the generation of hydroxyl radicals.[43]

$$(CH_3)_2SO + OH^{\bullet} \rightarrow CH_3(OH)SO + {}^{\bullet}CH_3 \quad (1)$$

$${}^{\bullet}CH_3 + DMPO \rightarrow {}^{\bullet}DMPO\text{–}CH_3 \quad (2)$$

The EPR studies clearly demonstrate that RB-RLNPs are capable of producing both $OH^{\bullet}$ and $O_2^{\bullet-}$ upon X-ray irradiation. Production of $OH^{\bullet}$ and $O_2^{\bullet-}$ radicals can be explained by the cascade of Compton, photo, and Auger-electrons that are produced by the interaction of X-rays with lanthanide-doped RLNPs.[15–17] The electrons then react with an acceptor *i.e.* PS, water, DMSO, and oxygen, inducing ROS generation.

Superoxide radicals can be transformed to hydrogen peroxide, singlet oxygen and oxygen *via* intracellular superoxide dismutase-mediated reactions. Then the accumulation of hydrogen peroxide in cancer cells further undergoes a Fenton reaction and converts into more chemically reactive and highly toxic hydroxyl radicals.[44] Thus, $O_2^{\bullet-}$ generating nanosystems are appealing candidates for hypoxic PDT.

Conclusions

Herein, we developed $NaLuF_4$:20% Gd^{3+}, 3% Dy^{3+} RLNPs coated with mesoporous silica and loaded with the Rose Bengal or Merocyanine 540 for X-ray-induced ROS generation. Furthermore, significant ROS production was detected through the DPBF assay in only 5 minutes of irradiation time, illustrating the efficiency of the system. A combination of ABDA, DPBF, sodium azide and EPR assays were used to confirm these findings. DPBF and ABDA are probes which are commonly used to determine the efficiency of a PDT system. Even though DPBF is more sensitive to singlet oxygen than ABDA is, it is not selective for singlet oxygen. Thus, using only a DPBF assay to prove singlet oxygen generation can lead to misinterpreted results. EPR, however, can be used to identify the type of PDT mechanism and the radical species produced. The EPR results confirm that hydroxyl and superoxide anion radicals were the main ROS species produced. This study provides the demonstration that RB and MC540 loaded $NaLuF_4$:20% Gd^{3+}, 3% Dy^{3+} RLNPs systems have great potential for use in activating photodynamic therapy in hypoxic environments. With this in mind, studies to validate the X-ray activated PDT effects of the RLNP nanosystems are underway.

Conflicts of interest

There are no conflicts to declare.

Acknowledgements

A. N. is grateful to the German Research Foundation (DFG, agreement NS 6/1-1) for scholarship support. G. A. M. is grateful to NSERC for support through the Alexander Graham Bell CGS-D fellowship. J. A. C. is a Concordia University Research Chair in Nanoscience and is grateful to Concordia University for financial support. J. A. C. is grateful to the Natural Science and Engineering Research Council (NSERC) of Canada for the sustained support of his research. The authors would like to acknowledge the Howarth Lab at Concordia University for their help with BET measurements, and Robin Stein at the MC^2 facility of McGill University for help with EPR data acquisition.

References

1 R. Misra, K. Sarkar, J. Lee, V. J. Pizzuti, D. S. Lee, M. P. Currie, S. E. Torregrosa-Allen, D. E. Long, G. A. Durm, M. P. Langer, B. D. Elzey and Y. Y. Won, *J. Controlled Release*, 2019, **303**, 237–252.
2 B. Cline, I. Delahunty and J. Xie, *Wiley Interdiscip. Rev.: Nanomed. Nanobiotechnol.*, 2019, **11**, e1541.
3 G. D. Wang, H. T. Nguyen, H. Chen, P. B. Cox, L. Wang, K. Nagata, Z. Hao, A. Wang, Z. Li and J. Xie, *Theranostics*, 2016, **6**, 2295–2305.
4 S. Mallidi, S. Anbil, A. L. Bulin, G. Obaid, M. Ichikawa and T. Hasan, *Theranostics*, 2016, **6**, 2458–2487.
5 A. L. Bulin, C. Truillet, R. Chouikrat, F. Lux, C. Frochot, D. Amans, G. Ledoux, O. Tillement, P. Perriat, M. Barberi-Heyob and C. Dujardin, *J. Phys. Chem. C*, 2013, **117**, 21583–21589.
6 S. Espinoza, M. F. Volhard, H. Kätker, H. Jenneboer, A. Uckelmann, M. Haase, M. Müller, M. Purschke and T. Jüstel, *Part. Part. Syst. Charact.*, 2018, **35**, 1–8.
7 V. J. Pizzuti, R. Misra, J. Lee, S. E. Torregrosa-Allen, M. P. Currie, S. R. Clark, A. P. Patel, C. R. Schorr, Y. Jones-Hall, M. O. Childress, J. M. Plantenga, N. J. Rancilio, B. D. Elzey and Y. Y. Won, *ACS Biomater. Sci. Eng.*, 2019, **5**, 4776–4789.
8 S. Clement, W. Deng, E. Camilleri, B. C. Wilson and E. M. Goldys, *Sci. Rep.*, 2016, **6**, 1–9.
9 R. Naccache, Q. Yu and J. A. Capobianco, *Adv. Opt. Mater.*, 2015, **3**, 482–509.
10 L. Prodi, E. Rampazzo, F. Rastrelli, A. Speghini and N. Zaccheroni, *Chem. Soc. Rev.*, 2015, **44**, 4922–4952.

11 G. A. Mandl, D. Van der Heggen, D. R. Cooper, J. J. Joos, J. Seuntjens, P. F. Smet and J. A. Capobianco, *Nanoscale*, 2020, **12**, 20759–20766.
12 D. R. Cooper, J. A. Capobianco and J. Seuntjens, *Nanoscale*, 2018, **10**, 7821–7832.
13 A. L. Bulin, V. Andrey, B. Andrei, D. Amans, G. Ledoux and C. Dujardin, *Nanoscale*, 2015, **7**, 5744–5751.
14 C. Dujardin, D. Amans, A. Belsky, F. Chaput, G. Ledoux and A. Pillonnet, *IEEE Trans. Nucl. Sci.*, 2010, **57**, 1348–1354.
15 A. Kamkaew, F. Chen, Y. Zhan, R. L. Majewski and W. Cai, *ACS Nano*, 2016, **10**, 3918–3935.
16 J. Choi, G. Kim, S. Bin Cho and H. J. Im, *J. Nanobiotechnol.*, 2020, **18**, 1–23.
17 F. Ahmad, X. Wang, Z. Jiang, X. Yu, X. Liu, R. Mao, X. Chen and W. Li, *ACS Nano*, 2019, **13**, 10419–10433.
18 W. Chen and J. Zhang, *J. Nanosci. Nanotechnol.*, 2006, **6**, 1159–1166.
19 H. Chen, G. D. Wang, Y. J. Chuang, Z. Zhen, X. Chen, P. Biddinger, Z. Hao, F. Liu, B. Shen, Z. Pan and J. Xie, *Nano Lett.*, 2015, **15**, 2249–2256.
20 C. Hsu, S. Lin and C. A. Chang, *ACS Appl. Mater. Interfaces*, 2018, **10**, 7859–7870.
21 C. Frochot and S. Mordon, *J. Porphyrins Phthalocyanines*, 2019, **23**, 347–357.
22 D. van Straten, V. Mashayekhi, H. S. de Bruijn, S. Oliveira and D. J. Robinson, *Cancers*, 2017, **9**, 1–54.
23 L. Larue, A. Ben Mihoub, Z. Youssef, L. Colombeau, S. Acherar and J. C. André, *Photochem. Photobiol. Sci.*, 2018, **17**, 1612–1650.
24 J. Dang, H. He, D. Chen and L. Yin, *Biomater. Sci.*, 2017, **5**, 1500–1511.
25 X. Li, D. Lee, J. D. Huang and J. Yoon, *Angew. Chem., Int. Ed.*, 2018, **57**, 9885–9890.
26 T. Entradas, S. Waldron and M. Volk, *J. Photochem. Photobiol., B*, 2020, **204**, 111787.
27 Y. Tang, J. Hu, A. H. Elmenoufy and X. Yang, *ACS Appl. Mater. Interfaces*, 2015, **7**, 12261–12269.
28 T. Sabri, P. Pawelek and J. A. Capobianco, *ACS Appl. Mater. Interfaces*, 2018, **10**, 26947–26953.
29 M. J. Davies, *Methods*, 2016, **109**, 21–30.
30 J. Hesse, D. T. Klier, M. Sgarzi, A. Nsubuga, C. Bauer, J. Grenzer, H. Rene, M. Wislicenus, T. Joshi, M. U. Kumke and H. Stephan, *ChemistryOpen*, 2018, 159–168.
31 National Center for Biotechnology Information, *PubChem Compd. Summ. CID 5901322; Merocyanine 540*, 2020, Retrieved Oct. 17; 2020 from https//pubchem.ncbi.nlm.nih.gov/compound/Merocyanine-540.
32 National Center for Biotechnology Information, *PubChem Compd. Summ. CID 32343, Bengal Rose B sodium salt*, 2020, Retrieved Oct. 17, 2020 from https//pubchem.ncbi.nlm.nih.gov/compound/Bengal-Rose-B-sodium-salt.
33 W. Fan, P. Huang and X. Chen, *Chem. Soc. Rev.*, 2016, **45**, 6488–6519.
34 X. Zhong, X. Wang, G. Zhan, Y. Yao, Z. Dong, L. Hou, H. Zhao, S. Zeng, J. Hu, L. Cheng and X. Yang, *Nano Lett.*, 2019, **19**, 8234–8244.
35 N. Miyoshi, M. Ueda, Y. Tanimoto, M. Itoh, K. Fuke and G. Tomita, *Z. Naturforsch., B: J. Chem. Sci.*, 1982, **37**, 649–652.
36 T. Sarna, J. Zajac, M. K. Bowman and T. G. Truscott, *J. Photochem. Photobiol., A*, 1991, **60**, 295–310.
37 M. Rózanowska, J. Ciszewska, W. Korytowski and T. Sarna, *J. Photochem. Photobiol., B*, 1995, **29**, 71–77.
38 A. Harriman, L. C. T. Shoute and P. Neta, *J. Phys. Chem.*, 1991, **95**, 2415–2420.
39 G. R. Buettner and B. E. Britigan, *Free Radical Biol. Med.*, 1990, **8**, 57–60.
40 J. L. Clément, N. Ferré, D. Siri, H. Karoui, A. Rockenbauer and P. Tordo, *J. Org. Chem.*, 2005, **70**, 1198–1203.
41 E. Finkelstein, G. M. Rosen and E. J. Rauckman, *Arch. Biochem. Biophys.*, 1980, **200**, 1–16.
42 G. R. Buettner, *Free Radical Biol. Med.*, 1987, **3**, 259–303.
43 L. Baptista, E. Clemente Da Silva and G. Arbilla, *Phys. Chem. Chem. Phys.*, 2008, **10**, 6867–6879.
44 M. Li, J. Xia, R. Tian, J. Wang, J. Fan, J. Du, S. Long, X. Song, J. W. Foley and X. Peng, *J. Am. Chem. Soc.*, 2018, **140**, 14851–14859.